Mantle plumes are oxidised

Yves Moussallam, Marc-Antoine Longpré, Catherine Mccammon, Alejandra Gómez-Ulla, Estelle F. Rose-Koga, Bruno Scaillet, Nial Peters, Emanuela Gennaro, Raphael Paris, Clive Oppenheimer

Mantle plumes are oxidised

Yves Moussallam[1,2], Marc-Antoine Longpré[3], Catherine McCammon[4], Alejandra Gomez-Ulla[1], Estelle F. Rose-Koga[1], Bruno Scaillet[5], Nial Peters[6], Emanuela Gennaro[7], Raphael Paris[1], Clive Oppenheimer[6]

[1] *Université Clermont Auvergne, CNRS, IRD, OPGC, Laboratoire Magmas et Volcans, F-63000 Clermont-Ferrand, France*

[2] *Lamont-Doherty Earth Observatory, Columbia University, New York, USA*

[3] *School of Earth and Environmental Sciences, Queens College, City University of New York, Queens, NY 11367, USA*

[4] *Bayerisches Geoinstitut, University of Bayreuth, D-95440 Bayreuth, Germany*

[5] *ISTO, UMR 7327, Université d'Orléans-CNRS-BRGM, 1A rue de la Férollerie, 45071 Orléans cedex 2, France*

[6] *Department of Geography, University of Cambridge, Downing Place, Cambridge, CB2 3EN, UK*

[7] *Istituto Nazionale di Geofisica e Vulcanologia, Sezione di Palermo, Via Ugo La Malfa, 153, 90146 Palermo, Italy*

Corresponding author: Yves Moussallam; yves.moussallam@gmail.com

Keywords: oxygen fugacity; degassing; XANES; melt inclusions; mantle plumes

ABSTRACT

From oxic atmosphere to metallic core, the Earth's components are broadly stratified with respect to oxygen fugacity. A simple picture of reducing oxygen fugacity with depth may be disrupted by the accumulation of oxidised crustal material in the deep lower mantle, entrained there as a result of subduction. While hotspot volcanoes are fed by regions of the mantle likely to have incorporated such recycled material, the oxygen fugacity of erupted hotspot basalts had long been considered comparable to slightly more oxidised than that of mid-ocean ridge basalt (MORB) and more reduced than subduction zone basalts. Here we report measurements of the redox state of glassy crystal-hosted melt inclusions from tephra and quenched lava samples from the Canary and Cape Verde Islands, that we can independently show were entrapped prior to extensive sulfur degassing. We find high ferric iron to total iron ratios ($Fe^{3+}/\sum Fe$) of up to 0.27–0.30, indicating that mantle plume primary melts are significantly more oxidised than those at mid-ocean ridges and even subduction zone contexts. These results, together with previous investigations from the Erebus, Hawaiian and Icelandic hotspots, confirm that mantle upwelling provides a return flow from the deep Earth for components of oxidised subducted lithosphere and suggest that highly oxidised material accumulates or is generated in the lower mantle. The oxidation state of the Earth's interior must therefore be highly heterogeneous and potentially locally inversely stratified.

I. INTRODUCTION

Temperature, pressure, volatile content, major element composition and oxygen fugacity (f_{O2}) are the five parameters controlling the occurrence and extent of partial melting in Earth's mantle, ultimately dictating where magmatic activity occurs on our planet. Of those, variables, oxygen fugacity of the mantle remains the least constrained yet its influence on phase relationship, volatile speciation, element partitioning and mantle physical properties is primary (e.g., Arculus, 1985). In terrestrial rocks, oxygen fugacity varies by over nine orders of magnitude (e.g., Parkinson and Arculus, 1999), but it remains to be seen how much oxygen fugacity varies in the upper mantle, especially in regions where melting occurs and if indeed systematic differences exist between tectonic contexts.

Our understanding of the oxygen fugacity of the upper mantle feeding volcanoes and their magmatic systems has been largely derived from measurements of the oxidation state (expressed as the $Fe^{3+}/\sum Fe$ ratio) of erupted basalts (e.g., Christie et al., 1986; Carmichael, 1991; Bezos and Humler, 2005; Rhodes and Vollinger, 2005; Cottrell and Kelley, 2011). Basaltic lavas sampled at hotspot volcanoes (e.g., Mallmann and O'Neill, 2009; Rhodes and Vollinger, 2005; Roeder et al., 2003) have an oxidation state typically more reduced than basaltic lavas from subduction zone volcanoes and comparable to that of global mid-ocean ridge basalt (MORB), implying that the oxygen fugacity of mantle plumes is similar to that of the mantle feeding MORB, i.e., near the fayalite–magnetite–quartz (FMQ) oxygen buffer (e.g., Bezos and Humler, 2005; Birner et al., 2018; Cottrell and Kelley, 2011; O'Neill et al., 2018; Zhang et al., 2018). However, it has become increasingly clear, from both theoretical considerations (e.g., Anderson and Wright, 1972; Burgisser and Scaillet, 2007; Métrich et al., 2009; Gaillard et al., 2011, 2015) and observations (e.g., Anderson and Wright, 1972;

Carmichael and Ghiorso, 1986; Kelley and Cottrell, 2012; Moussallam et al., 2014, 2016; Helz et al., 2017; Brounce et al., 2017; Longpré et al., 2017), that the oxygen fugacity of mantle melts can be strongly affected by the degassing of volatiles (especially sulfur) during magma ascent to the surface. While this effect can be minor for MORB magmas erupted under high hydrostatic pressure (e.g., Shorttle et al., 2015), it may be significant for shallow submarine and subaerial eruptions of hotspot volcanoes. Investigation of the oxygen fugacity of the upper mantle feeding hotspot volcanoes therefore demands identification and study of un-degassed melts that preserve the oxidation state acquired in equilibrium with the mantle.

In this work, we examine a series of olivine-hosted melt inclusions, embayments and matrix glasses from tephra and lava ballon samples erupted at the hotspots of the Canary (El Hierro and Lanzarote volcanoes) and Cape Verde (Fogo volcano) Islands whose mantle plume origin from the lower mantle is demonstrated from geophysical observations (French and Romanowicz, 2015). Melt inclusions represent samples of the melt taken at various stages during the degassing process, and previous investigations at these volcanoes have highlighted the presence of volatile-rich melt inclusions entrapped at depths exceeding 10 km (Gómez-Ulla, 2018; Longpré et al., 2017) and little affected by sulfur degassing. We report here on measurements of the oxidation state of these melt inclusions obtained by X-ray absorption near-edge structure (XANES) spectroscopy at the iron K-edge.

Throughout the text, melt fO_2 is calculated from $Fe^{3+}/\sum Fe$ using Equation 7 from Kress and Carmichael (1991) and ΔFMQ refers to the difference in fO_2 between the melt and the Fayalite-Magnetite-Quartz (FMQ) mineral redox buffer as reported in Frost (1991).

II. SAMPLES AND METHODS

Olivine-hosted melt inclusions, matrix glasses and embayments from rapidly-quenched tephra and lava balloon samples collected from the 1824 Lanzarote, 2011-2012 El Hierro, as well as tephra samples from Fogo volcano were polished on both sides to obtain doubly-exposed wafers with at least a 10 x 10 μm obstruction-free area through the inclusion. The analysed melt inclusions vary in minimum size from 36 to 181 μm in diameter (Table S1) and consist of brown-coloured transparent glass of ovoid shape (Fig. S1).

Two samples from Fogo volcano eruption were used in this study. The first (Fogo05) was collected on the western part of the Bordeira caldera wall at lat 14.936°; long -24.391°; 2190 m asl and consists of amalgamated tephra (poorly sorted, coarse-ashto fine-lapilli size) with abundant orthopyroxene (up to 15%) and rare olivine phenocrysts. The second (Fogo11) was collected on the western part of the Bordeira caldera wall at lat 14.937°; long -24.392°; 2340 m asl and consists of nearly aphyric (small pyroxenes and very rare olivine) phreatomagmatic tephra (moderately sorted, medium-to-coarse ash size) deposits. Tephra from “Volcan de Tao” (TAO) 1824 eruption at Lanzarote were used in this study (lat 29.03C; long -13.63V). Tephra are highly vesiculated (50–60 vol%), fine to coarse lapilli in size, with olivine phenocrysts ranging from 5 to 10% and trace amounts of clinopyroxene and plagioclase (see details in Gómez-Ulla, 2018). Samples from El Hierro (EH) used in this study came from seawater-quenched lava balloons, with shell ≤5 cm thick collected at lat 27.697°; long -17.993°. The lavas contains olivine, clinopyroxenes and Fe-Ti oxides (see details in Longpré et al., 2017).

2.1 XANES data acquisition

All samples were analysed on Beamline I18 at the Diamond Light Source (DLS) using Fe K-edge XANES (X-ray absorption near-edge structure spectroscopy). The X-rays were focused

with Kirkpatrick-Baez mirrors down to 2 µm (horizontal) × 1.2 µm (vertical) beam size. The beamline utilises a liquid nitrogen-cooled double-crystal monochromator with silicon crystals and the Si (333) reflection was used to increase the energy resolution. Measurements were performed in fluorescence mode, where we used two energy-dispersive Vortex ME-4 silicon drift detectors positioned at 45 degrees to the incident beam (one located directly above the other and pointing towards the sample). The sample was positioned so that the normal to the sample surface was at 45 degrees to the incident X-ray beam. Default analytical conditions for XANES at I18 yield a photon flux of 10^{10} ph/s by attenuating (using a combination of aluminium foils and slit) a 10^{12} ph/s primary beam upstream of the ion chamber. The beam can then be further attenuated (using Al foil). For melt inclusions, the incident X-ray beam was additionally filtered with an Al foil of 0.25 mm thickness to remove the effect of beam damage on the sample (see section below). Matrix glasses, which are water-poor, were analysed using an additional 0.1 mm Al foil attenuation. The energy step sizes and dwell times used are given in Table S2. For melt inclusions, two spectra were acquired and co-added for each analysis. All XANES spectra of melt inclusions were examined for contamination from the olivine host. Spectra showing any structure in the edge and post-edge region were rejected (see Fig. S6 in Moussallam et al., 2014 for an example of contaminated spectra).

2.2 Beam damage

The effect of sample exposure to focused beams of X-rays on iron speciation has been investigated in several studies under a range of beam and sample conditions (e.g., Cottrell et al., 2018, 2009; Moussallam et al., 2016, 2014; Shorttle et al., 2015). These works showed that the stronger the photon flux and the more water-rich the sample, the higher the amount of photo-oxidation. Accordingly, we performed a series of tests in order to determine the analytical conditions required to avoid beam damage for our samples.

We used a hydrated experimental glass of basaltic composition (49.36 wt.% SiO_2, 1.47 wt.% TiO_2, 14.36 wt.% Al_2O_3, 8.61 wt.% FeO, 0.16 wt.% MnO, 9.08 wt.% MgO, 11.71 wt.% CaO, 3.26 wt.% Na_2O, 1.3 wt.% K_2O) with a $Fe^{3+}/\sum Fe = 0.22$ (obtained using the Smithsonian basalt glass calibration and Zhang et al., (2018) $Fe^{3+}/\sum Fe$ values from Mössbauer spectroscopy and under the beam damage-free analytical conditions described below). This glass was chosen because it contains 5.2 wt.% H_2O (as determined by SIMS), which is considerably more than any of the natural glasses analysed subsequently, hence it represents a worst-case scenario in terms of beam damage. We positioned the monochromator at a fixed energy of 7114.3 eV, corresponding to the oxidised peak of the pre-edge doublet. We then opened the shutter and counted the fluoresced X-rays every second for 1000 sec (~17 min) (Fig. 1). This beam damage test was popularised by Shorttle et al., (2015) and further used by Cottrell et al., (2018) and has the advantage over the more classic repeated quick-scan approach (e.g., Moussallam et al., 2016, 2014; Wilke et al., 2008) to allow identification of any beam damage occurrence over the first seconds of sample-beam interaction. We found that, under our analytical conditions and using an Al foil of 0.25 mm that attenuates the beam to about 1% of its original flux (calculated based on theoretical absorption, equivalent to ~10^8 photon/s or ~10^7 to 10^8 photon/s/μm^2), no change in fluoresced intensity was recorded under beam exposure. By contrast, using a 0.10 mm Al foil or no attenuation at all produced significant photo-oxidation of the iron. These results indicate that Fe in our natural samples, measured using a 0.25 mm Al foil, was not oxidised during XANES analyses. Note that conditions at each synchrotron beamline are slightly different, so the conditions under which we observe no resolvable beam damage at I18 are entirely reproducible but not directly transposable to another synchrotron/beamline. In the same way that calibration with glass standards is required before

each XANES analytical session, we recommend that a beam damage test and identification of beam damage-free analytical conditions be performed before each XANES analytical session.

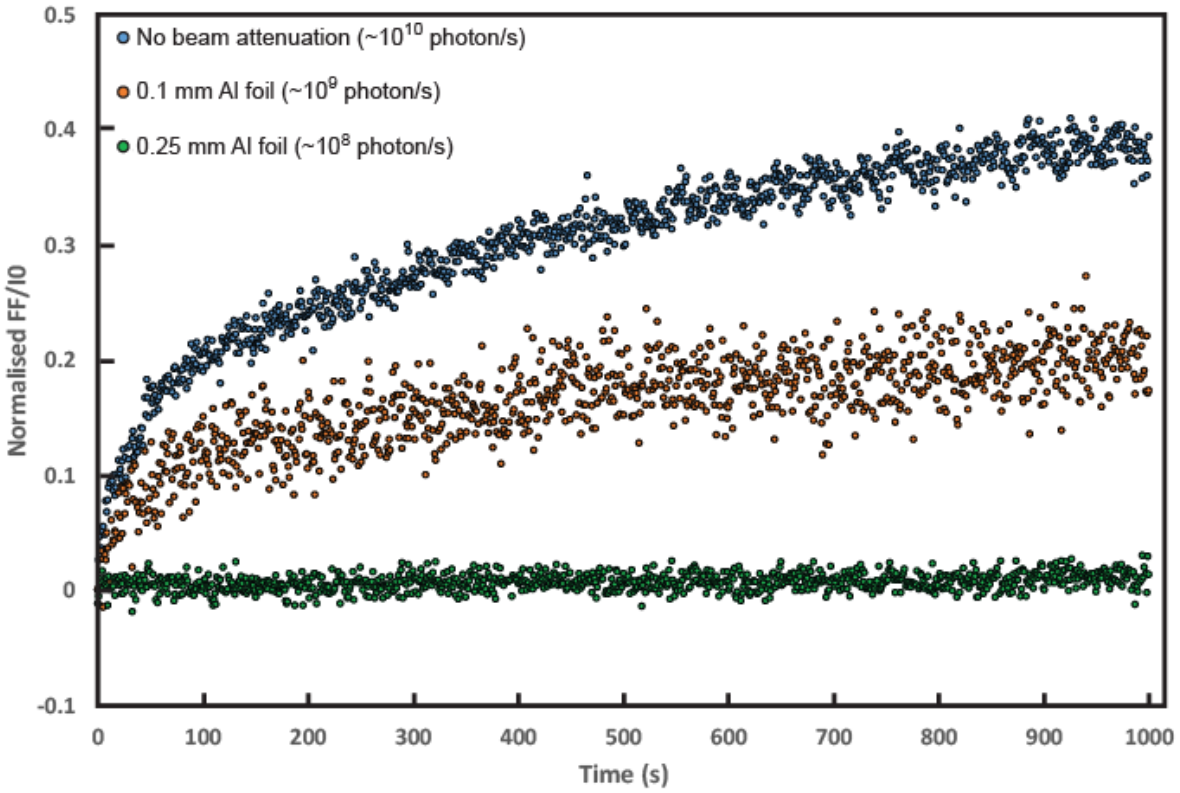

Figure 1*: Time series of normalised fluoresced intensity (FF) over I_0 at 7114.3 eV integrated over 1 s intervals for a hydrated (5.2 wt.% H_2O) basaltic glass under three different beam attenuation conditions. A fresh spot was illuminated with a 2.5 x 1.2 µm^2 beam for each analysis. While photo-oxidation can clearly be seen with no beam attenuation and with an attenuation down to about 16% of the original beam flux (using a 0.1 mm Al foil), no photo-oxidation can be detected once the beam has been attenuated down to 1% of its original flux (using a 0.25 mm Al foil). Note that in order to improve the signal/noise level during the test with a 0.25 mm Al foil, the detectors were moved closer to the (another time series acquired on another spot without the detector adjustment is shown in Fig. S5).*

178 **2.3 Standards and Mössbauer spectroscopy**

179 Glass standards for the XANES analyses were prepared in a controlled atmosphere furnace at
180 the Department of Earth Sciences, University of Cambridge using a controlled CO_2-CO gas
181 mixture. For each experiment, 50 mg of sample was placed in a platinum crucible. The sample
182 was then introduced into the furnace and heated at 1400°C and left to equilibrate for two hours.
183 At the end of each experiment, rapid quenching preserved chemical equilibrium as the sample
184 dropped into a container of deionised water. The drop was initiated by short-circuiting the thin
185 platinum wire by passing a current through the thick platinum wires. Six basanite standards of
186 2011-2012 El Hierro magma composition (44.4 wt.% SiO_2, 5.0 wt% TiO_2, 13.7 wt.% Al_2O_3,
187 12.5 wt.% FeO_t, 0.2 wt.% MnO, 8.1 wt.% MgO, 10.7 wt.% CaO, 3.5 wt.% Na_2O, 1.4 wt.%
188 K_2O and 0.5 wt.% P_2O_5) were equilibrated at various fO_2 conditions (FMQ–1, FMQ, NNO,
189 NNO+0.5, NNO+1 and NNO+1.5). All experiments were performed twice; first, in order to
190 equilibrate the Pt crucible with Fe at each fO_2 (during 24h) and, second, to produce the glass
191 used as standard. All standard glasses were subsequently analysed by electron microprobe. A
192 20-point electron microprobe transect was made across each standard to ensure all samples
193 were homogeneous and that neither iron nor sodium loss had occurred.
194
195 All basanite glass standards were analysed for $Fe^{3+}/\Sigma Fe$ by Mössbauer spectroscopy at the
196 Bayerisches Geoinstitut. Samples were analysed at room temperature using a constant
197 acceleration Mössbauer spectrometer in transmission mode with a nominal 370 MBq ^{57}Co
198 point source in a 12 μm Rh matrix. The active dimensions of the point source were 500 x 500
199 μm. The velocity scale was calibrated relative to α-Fe and line widths of 0.36 mm/s were
200 obtained for the outer lines of α-Fe at room temperature. Fits to Mössbauer spectra were
201 performed using MossA (Prescher et al., 2012) according to the approach used by Zhang et al.
202 (2018) (xVBF model). A linear baseline was added to account for the shadowing effect and all

fits used the full transmission integral to account for thickness effects of source and absorber (Rancourt, 1989). Conventional constraints (doublet components with equal widths and areas) were used and $Fe^{3+}/\Sigma Fe$ ratios were determined from the relative areas corrected for recoil-free fraction effects according to Zhang et al. (2018). All Mössbauer spectra are shown in Fig. S2 and values are reported in Table S3.

2.4 XANES spectra processing, $Fe^{3+}/\sum Fe$ calibration and data quality

As stated above, in order to avoid any beam damage and photo-oxidation of iron under the X-ray beam, all analyses of melt inclusions were performed using a highly attenuated beam (1% of initial photon flux). These analytical conditions resulted in acquired spectra of lower quality than typical for XANES analyses at the Fe K-edge (examples of such spectra are shown in Fig. 2). Noise in the acquired spectra made typical fitting of the pre-edge region with a combination of a linear function and a damped harmonic oscillator function (DHO), and subsequent centroid determination (e.g., Wilke et al., 2001; Farges, 2001; Berry et al., 2003; Wilke et al., 2004; Cottrell et al., 2009; Moussallam et al., 2014) imprecise. To circumvent this problem, we used the ratio of the pre-edge peak heights, on which we found spectra quality had a lesser effect, to derive $Fe^{3+}/\sum Fe$ from natural spectra. In detail, the pre-edge region was still fitted with a combination of a linear function and a damped harmonic oscillator function (DHO) but instead of determining the centroid we measured the relative height of the 1s→3d pre-edge feature absorption multiplet peaks. The peak height ratio was then parameterised against the Fe valence state using our basanite glasses standards (Fig. 3).

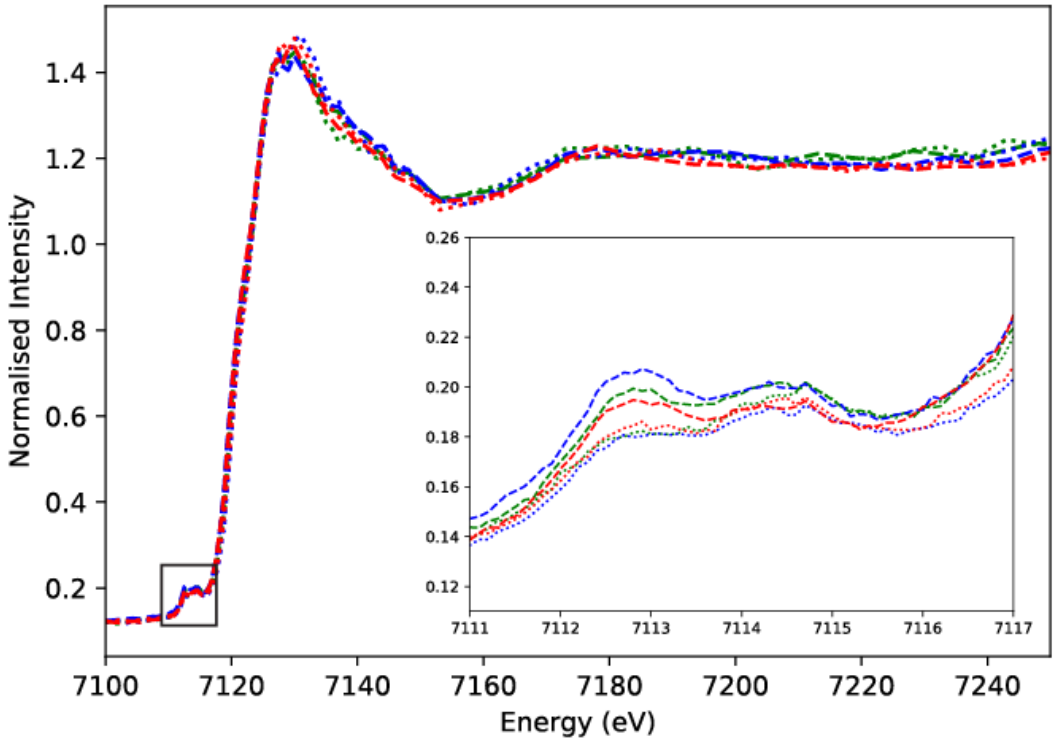

***Figure 2**: Example of edge-step normalised XANES spectra (two co-add) obtained using a 0.25 mm Al plate attenuation. Spectra from both more oxidised (dashed lines) and more reduced (dotted lines) melt inclusions are shown for El Hierro (red), Lanzarote (blue) and Fogo (green) volcanoes.*

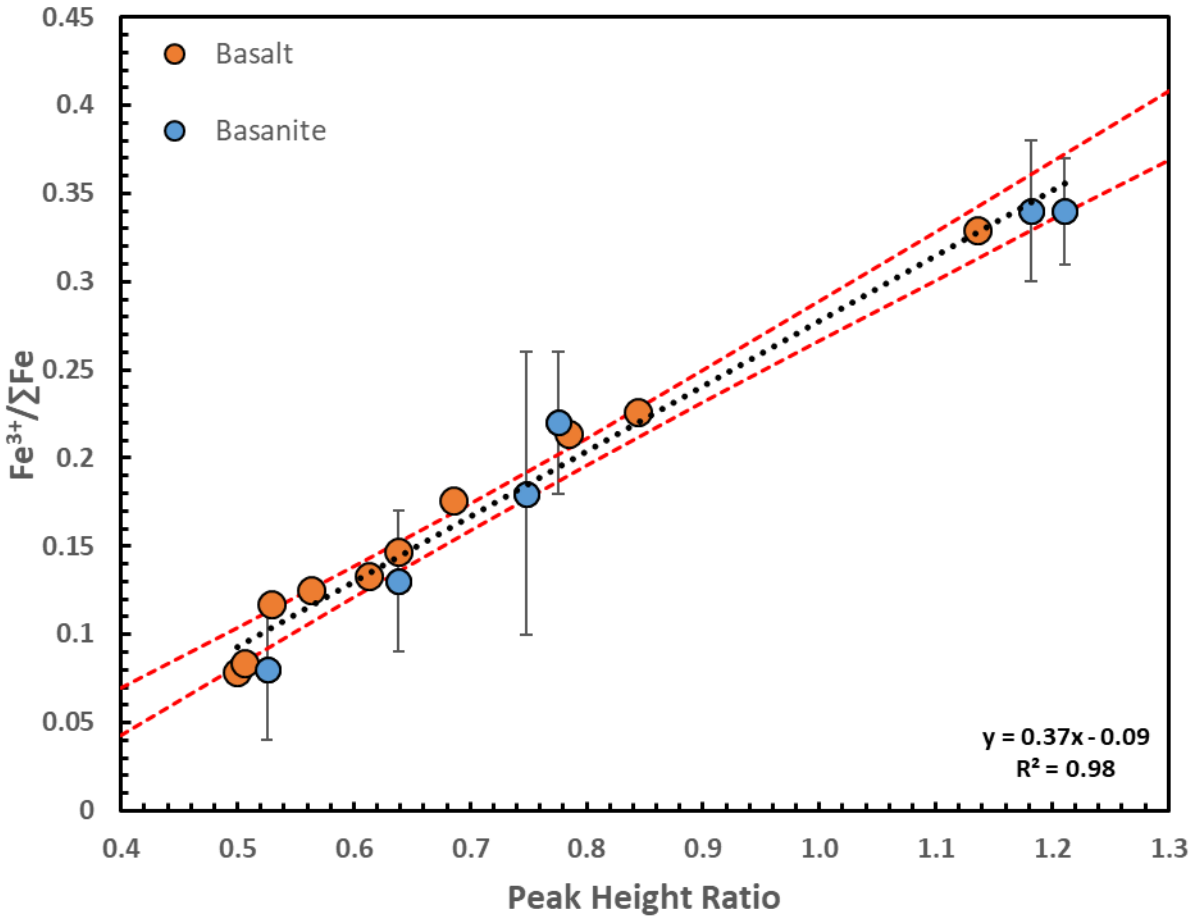

230

231 ***Figure 3****: : Calibration line of the peak height ratio determined by XANES compared with the*
232 *$Fe^{3+}/\sum Fe$ ratios determined by Mössbauer spectroscopy in basanite standard glasses (this*
233 *study) and basaltic standard glasses from the Smithsonian (Mössbauer values from* Zhang et
234 al., (2018)*). A linear regression through the basanite and basalt standards data (dotted black*
235 *line) yields an equation of y = 0.37x – 0.09 with an R^2 of 0.98, a P-value of $1.6x10^{-6}$ and a*
236 *standard error on the regression of 0.013. Dashed red lines show 95% confidence intervals.*
237 *Note that the relationship between the peak height ratio and $Fe^{3+}/\sum Fe$ is well captured by a*
238 *linear regression for $Fe^{3+}/\sum Fe$ between 0.1 and 0.4 (see supplementary Fig. S6), in agreement*
239 *with previous studies (e.g.,* Cottrell et al., 2009*).*

240

241 In order to estimate the effect of lower quality spectra on the estimation of the peak height ratio
242 we compared the ratio obtained from the processing of two co-added low quality spectra

produced with a 0.25 mm Al plate attenuation to the ratio retrieved from normal high quality spectra obtained with 0.1 mm Al plate attenuation for twelve basaltic Smithsonian standards (Fig. S3). The standard deviation between these analyses was used to determine the error on the peak height ratio ($1\sigma = 0.03$) which translates to a standard deviation of 0.012 on the measured $Fe^{3+}/\sum Fe$ ratio. Note that this is the relative error from XANES analyses, the absolute error in term of $Fe^{3+}/\sum Fe$ is given by the standard error on the calibration curve ($1\sigma = 0.013$). Matrix glasses were acquired with lower attenuation (0.1 mm Al plate) and hence processed using the more commonly used centroid method (e.g., Cottrell et al., 2009; Moussallam et al., 2016, 2014).

2.5 Major elements and volatile analyses

Major and volatile (S, Cl, and F) element concentrations were measured on a Cameca SX-100 electron microprobe at the Laboratoire Magmas et Volcans, in Clermont-Ferrand using an accelerating voltage of 15 keV, a beam current of 6 nA for major elements and 40 nA for volatiles with a 10 μm spot diameter. Sodium was analysed first to prevent Na loss. The counting time was 10 s for Na, Ca, Ti, P and Si, 20 s for Mg and Al, 30 s for Mn and finally 40 s for Fe and K. The instrument was calibrated on natural and synthetic mineral standards and glasses. The Kilauea basaltic glass VG-A99 (Jarosewich et al., 1979) and a pantellerite glass from Eburru Kenya KE12 (Mosbah et al., 1991), which are all international glass standards, were used as an inter-laboratory check for major element, S and Cl and F concentrations, respectively.

H_2O and CO_2 concentrations were determined by FTIR spectroscopy using a Vertex 70 Bruker spectrometer equipped with an infrared microscope (Hyperion) and an MCT detector at the Laboratoire Magmas et Volcans, in Clermont-Ferrand. Absorption spectra were acquired with

128 scans in the near-infrared region at a resolution of 4 cm^{-1}. The total amount of water was calculated from the absorbance of the fundamental OH-stretching vibration at about 3535 cm^{-1} while the amount of CO_2 was calculated using the "carbonate doublet" (Blank and Brooker, 1994) at 1515 and 1430 cm^{-1}. The sample thickness was measured on a Raman microscope and background correction (using a cubic function for CO_2 and a linear function for H_2O) was performed using PeakFit software (Jandel Scientific) to measure absorption peak heights. We used molar absorptivity values for basanite from Shishkina et al., (2014). Melt inclusions major and volatile compositions are given in Tables S4 and S5.

2.6 Assessment of post-entrapment modification of melt inclusions.

2.6.1 Post-entrapment crystallisation

The amount of post-entrapment crystallisation was estimated using the Petrolog3 software (Danyushevsky and Plechov, 2011). Calculations were performed using the olivine-melt model of Danyushevsky, (2001), the density model of Lange and Carmichael, (1990), the model for melt oxidation of Kress and Carmichael, (1988) and the model of Toplis, (2005) for the compositional dependence of the olivine-liquid Fe-Mg exchange coefficient (Kd). Note that calculations in Petrolog3 are performed under anhydrous conditions at 1 atm. Calculations were performed assuming a system closed to oxygen, in which case Fe^{3+} is treated as an incompatible element. The $Fe^{3+}/\sum Fe$ ratios measured by XANES were used to calculate Fe_2O_3 and FeO contents for each melt inclusion as input for the calculations.

Fig. 4 compares the measured Fo content of the host olivine to its expected value at equilibrium based on uncorrected melt inclusion composition. Most calculated olivine compositions agree with measured compositions within a few Fo% suggesting a limited amount of post-entrapment crystallisation or Fe-loss by re-equilibration. Another method to estimate if iron has been loss

from melt inclusions is to compare measured melt inclusion compositions to liquid lines of descent defined by published bulk rocks and glasses at each hotspot locality (Fig. S7). Using this method, we find that melt inclusions from Lanzarote and to a lesser extent, El Hierro, might have suffered some amount of iron loss. We consider this second method to be less accurate, however, as it assumes a co-genetic link between rock sequences that might be unrelated.

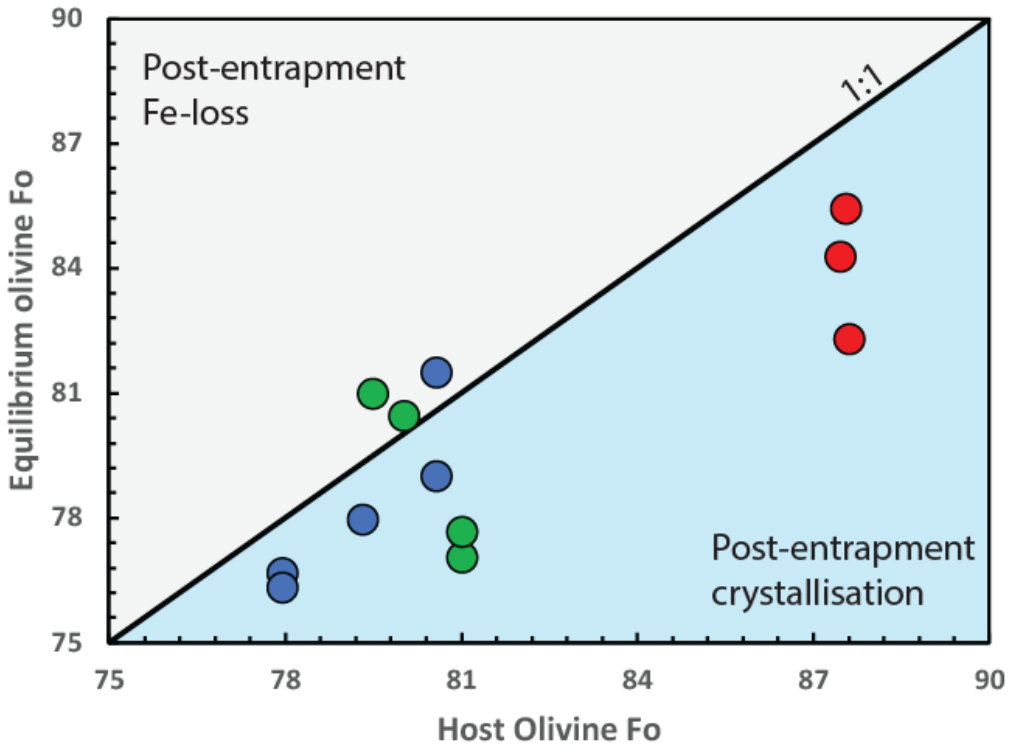

Figure 4: *Comparison between measured and equilibrium Fo content of host olivine for melt inclusions from Fogo (blue), El Hierro (green) and Lanzarote (red). Equilibrium Fo contents are calculated by Petrolog3 software (Danyushevsky and Plechov, 2011) using the model of Toplis, (2005) for the compositional dependence of the olivine-liquid Fe-Mg exchange coefficient (Kd).*

Since post-entrapment crystallisation and re-equilibration calculations are highly model dependent and current models of Fe-Mg exchange coefficient are not well calibrated for

basanite composition, we choose not to use PEC results from Petrolog3 to "correct" the measured oxidation state of iron in the melt inclusions. We note that the calculated amount of PEC from Petrolog3 is small (from 0 to 3.7%, average of 1.3%, median of 1%) and hence that the measured oxidation states of the melt inclusions are representative of the melt oxidation states at the time of entrapment. Post-entrapment crystallisation corrected compositions are reported in Table S7.

2.6.2 Volatile diffusion

Post-entrapment diffusion of volatiles either through the olivine host (for H) (Hauri, 2002; Massare et al., 2002) or in the vapor bubble (for CO_2) (Anderson and Brown, 1993; Steele-Macinnis et al., 2011) can modify the original volatile content of melt inclusions. As such, our measurements of H_2O and CO_2 can be considered as minimum estimates of the original amounts dissolved in the inclusions even though all of our samples are from rapidly quenched tephra and lava ballons. Higher (than measured) original H_2O and CO_2 contents of the melt inclusions would yield greater calculated entrapment pressures but would make no difference to the conclusions presented here. H diffusion out of a melt inclusion could, however, also have an impact on the oxidation state of the inclusion with a predicted increase of the oxidation state of the melt inclusion with increasing amount of H diffusion (some experiments have shown no effect (Rowe et al., 2007) while others found a complete re-equilibration with the groundmass (Bucholz et al., 2013; Gaetani et al., 2012)). Although this process cannot be ruled out, the opposite correlation between H_2O and oxidation state shown by previous datasets as well as ours (see Results section) strongly argues against this process dominating the observed data variability.

333 **2.7 Effect of differentiation**

334 Fig. S8 shows an absence of correlation between three proxies of melt differentiation and the
335 oxidation state of the melt, indicating that differentiation is not the dominant factor affecting
336 melt oxidation state in our data set. To assess the potential effect of pre-entrapment
337 crystallization of olivine on $Fe^{3+}/\sum Fe$, we modelled reverse crystallization paths for our melt
338 inclusions along olivine-control lines using PRIMELT3 (Herzberg and Asimow, 2015) until
339 the melts reached equilibrium with Fo_{90} olivine. The results shown in Fig. 5 and Table S8
340 indicate a modest decrease in $Fe^{3+}/\sum Fe$ with reverse crystallization, demonstrating that melts
341 parental to our melt inclusions were already oxidised.
342

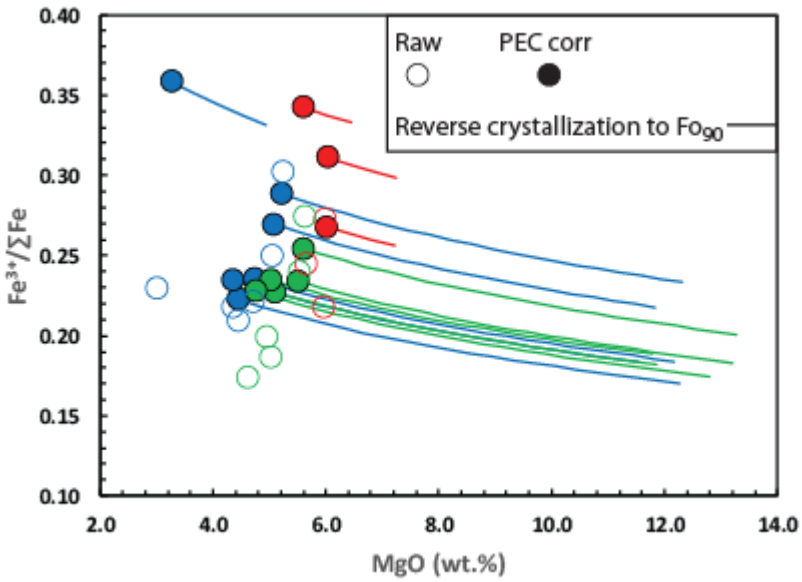

343

344 ***Figure 5:*** *Sensitivity analysis of the effects of post-entrapment crystallisation and pre-*
345 *entrapment crystallization of olivine on melt* $Fe^{3+}/\sum Fe$. *Post-entrapment crystallisation*
346 *estimated using Petrolog3 software (Danyushevsky and Plechov, 2011) assuming a system*
347 *closed to oxygen, with* Fe^{3+} *behaving incompatibly, leads to a decrease in* $Fe^{3+}/\sum Fe$ *in*
348 *corrected inclusions. The effect of pre-entrapment crystallization of olivine, modelled with*
349 *PRIMELT3* (Herzberg and Asimow, 2015) *until melt–*Fo_{90} *olivine equilibrium is reached, is*

shown to have modest effects on $Fe^{3+}/\sum Fe$ over large MgO ranges, suggesting that primary magmas were oxidised. Note that samples from Lanzarote (red) might have experienced Fe-loss (Fig. S9).

III. RESULTS

Melt inclusions from all three localities have $Fe^{3+}/\sum Fe$ ratios of 0.17 to 0.30 (with one sigma error of 0.012). These values are representative of the oxidation state of the melt at the time of entrapment and of their parental primitive magmas (see calculation of the effect of pre-entrapment processes in the methods section). The $Fe^{3+}/\sum Fe$ ratios of the melt inclusions do not correlate with major element composition (see methods section) but they are strongly correlated with volatile contents (Fig. 6 A to C). More volatile-rich melt inclusions, i.e., those entrapped at greater depths, are systematically more oxidised than their volatile-poor counterparts. This trend is even clearer when comparing our results with reported analyses for the Erebus (Moussallam et al., 2014), Icelandic (Hartley et al., 2017) and Hawaiian (Moussallam et al., 2016; Brounce et al., 2017) hotspots.

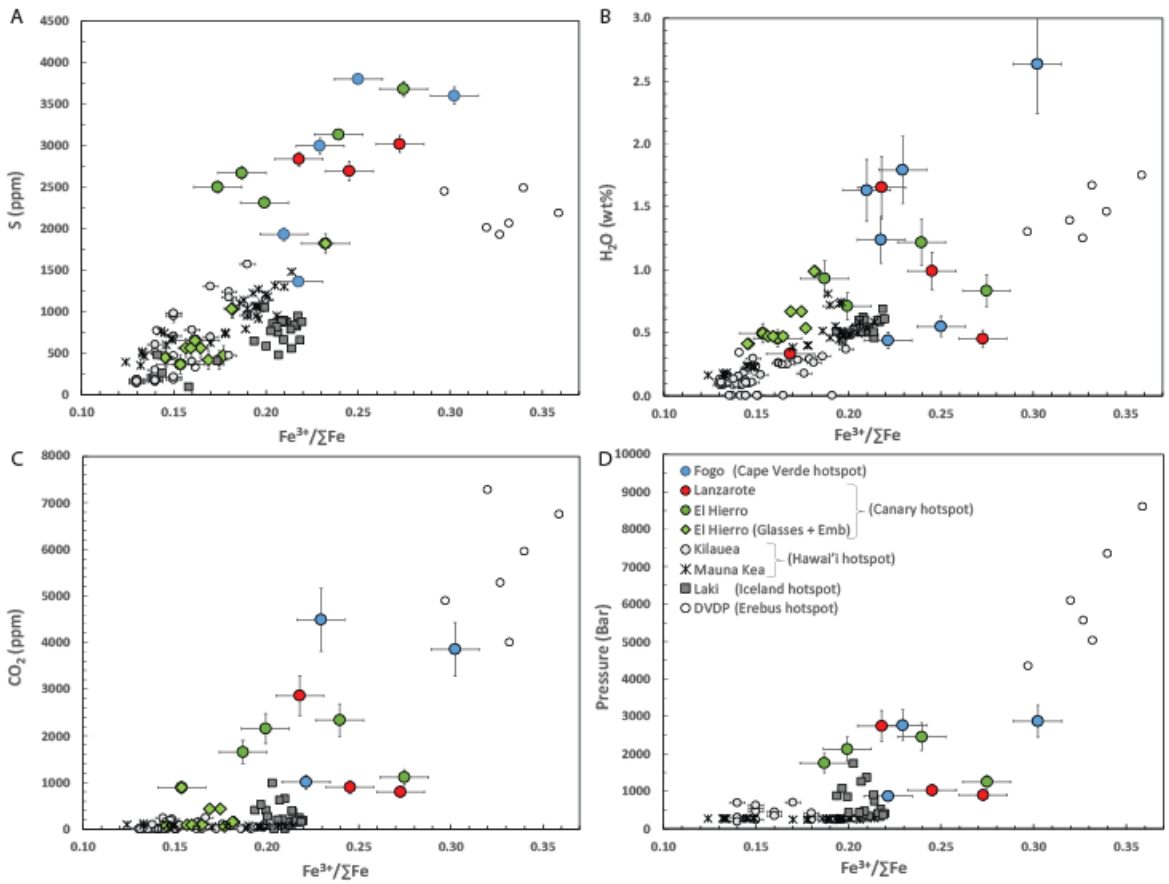

364

365 **Figure 6**: Volatile contents of melt inclusions, embayments and matrix glasses and
366 corresponding volatile saturation pressures, for Fogo, Lanzarote and El Hierro (this study) and
367 for Kīlauea (Moussallam et al., 2016), Mauna Kea (Brounce et al., 2017), Laki (Hartley et al.,
368 2017) and Erebus (Moussallam et al., 2014) versus $Fe^{3+}/\Sigma Fe$, determined by XANES. **A**. S
369 concentration (in ppm; determined by electron microprobe). **B**. H_2O concentration (in wt%;
370 determined by Fourier transform infrared spectroscopy). **C**. CO_2 concentration (in ppm;
371 determined by Fourier transform infrared spectroscopy). **D**. Calculated entrapment pressure
372 (using the model of Iacono-Marziano et al., 2012 and accounting for S in the data of this study),
373 with CO_2-H_2O saturation curves shown in the supplementary information. Note that
374 entrapment pressure estimates are always a minimum and that samples from Lanzarote might
375 have experienced Fe-loss.

IV. DISCUSSION

4.1 A case for oxidised mantle plumes

The most volatile-rich inclusions from El Hierro, Lanzarote and Fogo record $Fe^{3+}/\Sigma Fe$ ratios ranging from 0.27 to 0.30, corresponding to oxygen fugacities around 1.5 to 2 log units above the FMQ buffer. The only available comparable data, from very-deeply entrapped melt inclusions recording conditions prior to extensive degassing, are from Ross Island, Antarctica where similarly high oxygen fugacities have been found (Moussallam et al., 2014). The finding that all investigated hotspot volcanoes (El Hierro, Lanzarote, Fogo and Erebus), for which deeply-entrapped (> 8 km) melt inclusions are available, are associated with strongly oxidised primitive melts suggests a global relationship. This is corroborated by three other lines of evidence: (i) the observation of increasingly-oxidised MORB approaching hotspots such as Iceland (Shorttle et al., 2015); (ii) the abundance of S^{6+} in hotspot basalts (Brounce et al., 2017; Jugo et al., 2010); and (iii) the determination of slightly more oxidizing (up to FMQ+1) conditions in the least-degassed melt inclusions and glasses available from other hotspot volcanoes (Hawai'i (Brounce et al., 2017; Moussallam et al., 2016) and Iceland (Hartley et al., 2017)).

The most volatile-rich and deeply-entrapped melt inclusions should record conditions closest to the original mantle melt. From our dataset the effect of crystal fractionation on fO_2 appears to be minimal (see methods section). Even the most deeply-entrapped inclusions, however, likely experienced some amount of degassing. The original, pre-degassing, degree of oxidation of the melt can be estimated if we know how volatile-rich, especially how sulfur-rich, that melt was prior to degassing. Previous studies for Lanzarote (Gómez-Ulla, 2018) and El Hierro (Longpré et al., 2017) reported melt inclusions with sulfur contents of up to 3900 and 5000

401 ppm, respectively, while for Hawaii (at Lō‘ihi) sulfur contents of up to 3300 ppm have been
402 reported (Hauri, 2002). Extrapolating from our dataset, and in coherence with previous
403 degassing models (Moussallam et al., 2014), such sulfur contents would imply a mantle melt
404 oxygen fugacity about 2.0 log units above the FMQ buffer (Fig. 7), hence a mantle source about
405 two log units more oxidised than that feeding mid-ocean ridges (around FMQ; e.g., Berry et
406 al., 2018; Bezos and Humler, 2005; Birner et al., 2018, 2017; Bryndzia and Wood, 1990;
407 Cottrell and Kelley, 2011; Zhang et al., 2018). These estimates are also significantly more
408 oxidised than those inferred for primitive melts in the mantle wedge feeding arc magmas
409 (around FMQ+1; e.g., Bénard et al., 2018; Brandon and Draper, 1996; Parkinson and Arculus,
410 1999).
411
412 It should be noted that by equating the oxidation state of deep melts to that of their mantle
413 source we are assuming that melts are effectively buffered by their mantle source during partial
414 melting. For MORBs, several lines of evidence support this hypothesis; (i) the lack of
415 correlation between $Fe^{3+}/\Sigma Fe$ of MORB glasses and parameters sensitive to the degree of partial
416 melting (Bézos and Humler, 2005, Cottrell and Kelley, 2011), (ii) the similarity in measured
417 oxidation state of MORB glasses and co-located peridotites (Birner et al., 2018), and (iii)
418 experimental investigations of partial melting showing that the melt $Fe^{3+}/\Sigma Fe$ ratios remain
419 constant over varying degrees of partial melting (Sorbadere et al., 2018). In plume contexts it
420 is currently unknown if this assumption remains valid. The relationship between $Fe^{3+}/\Sigma Fe$ and
421 fO_2 in low-degree, volatile- and alkali-rich, partial melts is not well established, and it is
422 conceivable that partial melting in some contexts would operate as an open system favouring
423 the generation of Fe^{3+}-rich melts (Fe^{3+} being mildly incompatible during partial melting, e.g.,
424 Canil et al., 1994; Holloway and Burnham, 1972; Mallmann and O’Neill, 2009; Sorbadere et
425 al., 2018). Given the current lack of evidence of such open-system partial melting processes

taking place, we assume here that partial melting in plume contexts operates similarly to partial melting in mid-ocean ridge contexts in terms of oxidation state, and hence that the oxidation state of partial melts pre-degassing is similar to that of their source.

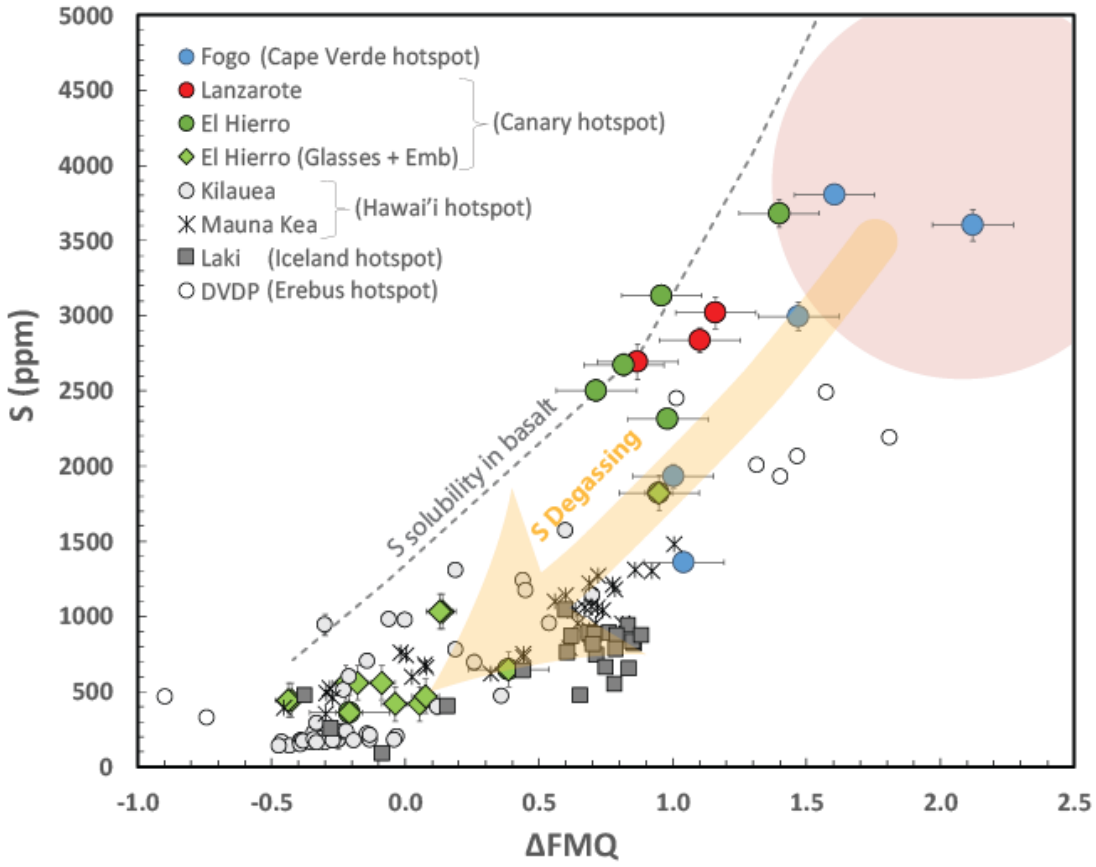

Figure 7: Sulfur contents of melt inclusions, embayments and matrix glasses from this study and for Kīlauea (Moussallam et al., 2016), Mauna Kea (Brounce et al., 2017), Laki (Hartley et al., 2017) and Erebus (Moussallam et al., 2014) compared with the oxygen fugacity of the melt expressed as the deviation from the fayalite–magnetite–quartz buffer. The pink shaded area represents inferred conditions of the primitive mantle melt feeding hotspots, extrapolated from the data trend to the maximum reported sulfur contents (of around 3000 to 5000 ppm) in melt inclusions from hotspot volcanoes. The light orange arrow shows the expected relationship between sulfur content and melt oxidation state due to sulfur degassing (e.g., Moussallam et al., 2014, 2016). The dashed grey line shows the maximum amount of sulfur that can be

dissolved at a given oxidation state in common basaltic melts at 200 MPa (Botcharnikov et al., 2011). Note that samples from Lanzarote might have experienced Fe-loss.

4.2 Recycling of oxidised subducted material

Mantle plumes, as the source of hotspot volcanism, might therefore be considerably more oxidised than their surrounding mantle. The simplest explanation for this phenomenon is that these plumes entrain recycled surface-derived material such as subducted oceanic crust. Indeed, isotopic and trace element evidence indicating the presence of recycled oceanic (and sometimes continental) crust in mantle plumes is abundant (Chauvel et al., 1992; Day et al., 2010; Gómez-Ulla et al., 2017; Hauri, 1996; Hofmann and White, 1982). In particular, helium, argon, lead and strontium isotopic ratios suggest that in both the Canary (e.g., Day and Hilton, 2011; Hiltona et al., 2000)) and Cape Verde (e.g., Christensen et al., 2001; Doucelance et al., 2003; Millet et al., 2008) hotspots a lower mantle and a HIMU component (interpreted as recycled subducted oceanic crust) must have mixed to explain the isotopic composition of extruded lavas. The observation that oxidised mantle melts in hotspot settings are also S-rich (Fig. 7) might additionally suggest the presence of recycled oceanic crust in their parental mantle since hydrothermally-altered crust is enriched in S (Alt et al., 1993), although multiple lines of evidence suggest that most of the S in the subducting slab might migrate to the mantle wedge, with potentially limited amounts being brought deep into the mantle (Bénard et al., 2018; Jégo and Dasgupta, 2014, 2013; Prouteau and Scaillet, 2013; Tomkins and Evans, 2015). An alternative mechanism to explain the oxidised nature of mantle plumes is the decomposition of subducted Fe_2O_3 from banded iron formations to Fe_3O_4 and $Fe_{25}O_{32}$ at pressures above ~60 and ~70 GPa, respectively (Bykova et al., 2016). This would generate an oxygen-rich fluid in the lower mantle that could be sampled by ascending plumes. Yet another possibility relies on pressure effects on iron coordination. It has been proposed that pyrite-structured iron oxide

464 (FeO_2 – referred to as P-phase) may form under extreme pressure and temperature in the Earth's
465 interior (Hu et al., 2016). If so, highly oxidised patches containing iron in the 3+ valence state
466 may accumulate in the deep lower mantle (Hu et al., 2017, 2016; Streltsov et al., 2017). Early
467 incorporation of such material into mantle plumes would result in decomposition to Fe_2O_3 and
468 release of O_2 during decompression (reaction 1 in Hu et al., 2016), providing an additional
469 mechanism for generation of oxidised hotspot conditions. The hypothesis we favour, the most
470 simple, is the incorporation of recycled surface-derived material in plumes.
471
472 **4.3 Implication for fO_2 stratification and partial melting in Earth's mantle**
473 Mantle plumes might therefore play a key role in the deep oxygen – and potentially S – cycles,
474 providing a counterflow to subduction zones, and channelling oxidised material out of the deep
475 Earth. The oxidised nature of mantle plumes might also partly explain their seismic velocity
476 structure. It has been shown that the seismic properties of olivine are highly dependent on iron
477 oxidation state, with olivine containing more Fe^{3+} showing enhanced anelastic relaxation (Ii et
478 al., 2018). The low-velocity anomalies found beneath hotspot volcanoes (e.g., French and
479 Romanowicz, 2015; Zhao, 2007) might then not only indicate elevated mantle temperatures
480 but also raised mantle oxygen fugacity.
481
482 While the geochemically-layered view of the Earth's mantle that prevailed in the twentieth
483 century has been progressively dismantled over the past four decades (e.g., White, 2015), our
484 picture of mantle oxidation state has remained mostly one-dimensional, i.e., fO_2 decreasing
485 steadily with depth (Frost and McCammon, 2008; Rohrbach and Schmidt, 2011; Woodland
486 and Koch, 2003). Our findings suggest that geochemical, geophysical and redox
487 heterogeneities should be linked in the Earth's mantle. A heterogeneous mantle in terms of
488 oxidation state implies that processes such as carbon redox melting (the production of

carbonated melts from the oxidation of CH_4 or native carbon (Taylor and Green, 1988; Foley, 2010; Rohrbach and Schmidt, 2011)) should occur over a wide range of depths in distinct regions of the mantle. Following Stagno et al., (2013), for instance, and considering that the mantle domains feeding hotspots are two log units more oxidised than those beneath mid-ocean ridges, redox melting associated with hotspots should prevail at much greater depths (Fig. 8), especially if these domains are also more carbon-rich.

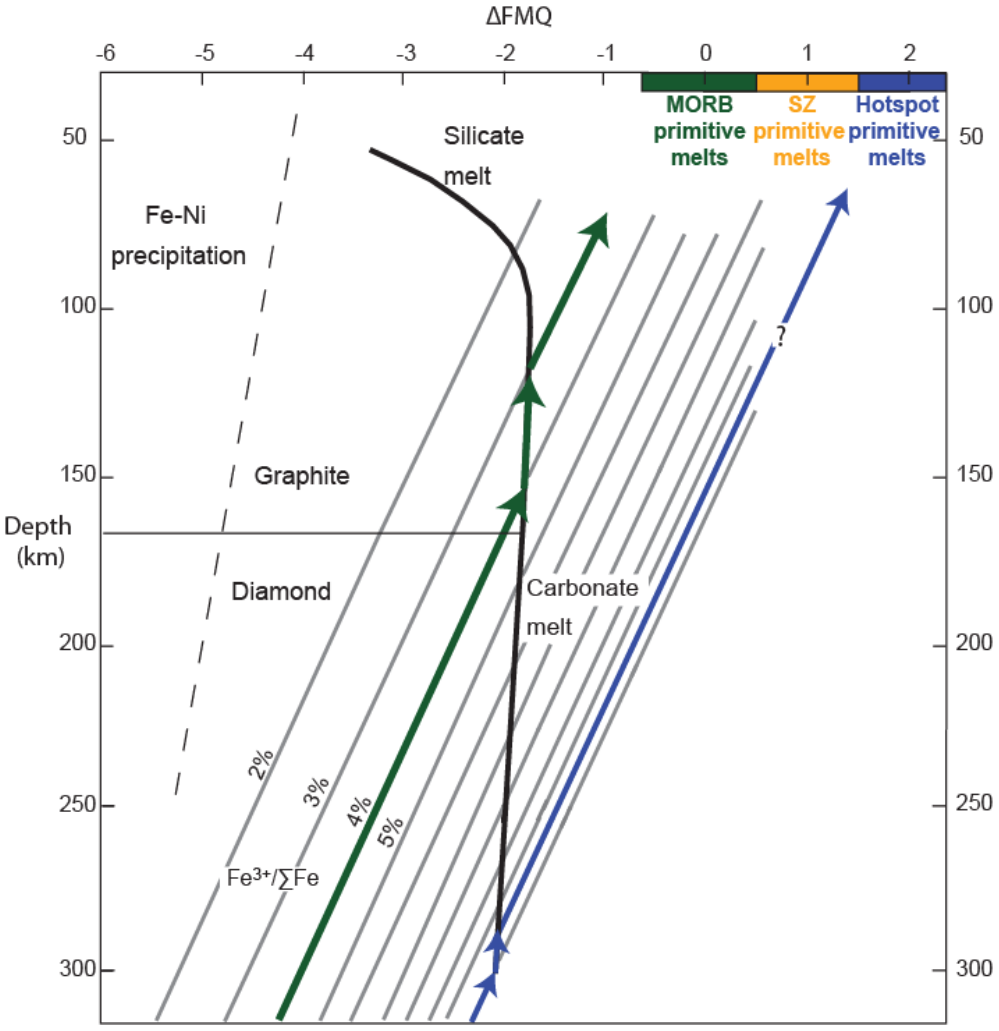

Figure 8: Relationship between depth and oxygen fugacity (expressed as the deviation from the FMQ buffer) for variable $Fe^{3+}/\sum Fe$ from Stagno et al., (2013). The stability fields of diamond and graphite are shown and bounded by the carbonate redox melting reaction line (thick black line). The green arrows (from Stagno et al., (2013)) show the expected evolution of an upwelling mantle with $Fe^{3+}/\Sigma Fe$ ratio of 0.04, initiating carbonate melting at ~150 km. The blue arrows show the expected evolution of an upwelling mantle with a $Fe^{3+}/\Sigma Fe$ ratio of

0.12, initiating carbonate melting at ~300 km depth. Both scenarios arbitrarily consider mantle sources with 30 ppm carbon (causing a reduction of the bulk rock $Fe^{3+}/\Sigma Fe$ ratio by 1% during redox melting). For greater carbon contents in the mantle sources (likely for hotspot mantle sources), a greater initial $Fe^{3+}/\Sigma Fe$ ratio is required for the oxygen fugacity to remain in the range estimated for MORB and hotspot sources. The relationship between $Fe^{3+}/\Sigma Fe$ ratio and oxygen fugacity for the mantle is calculated from equation 6 of Stagno et al., (2013) and differs from that for the melts (calculated using Kress and Carmichael, (1991)). The boxes for hotspot (this study and Moussallam et al., 2014), subduction zone (SZ) (e.g., Bénard et al., 2018; Brandon and Draper, 1996; Parkinson and Arculus, 1999) and MORB (e.g., Berry et al., 2018; Bezos and Humler, 2005; Christie et al., 1986; Zhang et al., 2018) primitive melts indicate oxidation state only (not depth).

V. CONCLUSION

We have investigated the redox state of glassy crystal-hosted melt inclusions in lavas of the Canary and Cape Verde Islands by XANES and compared them with similar measurements from Ross Island, Hawaii and Iceland. We showed that, at all five investigated hotspots to date, the apparently reduced state of erupted lavas is primarily acquired from degassing during magma ascent.

We found that the most deeply entrapped samples, i.e., those preserving mantle equilibrium conditions and found at the Canary, Cape Verde and Erebus hotspots, are highly oxidised. This leads us to infer that globally, present day mantle plumes might be up to two orders of magnitude more oxidised than mantle beneath mid-ocean ridges (that is fO_2 two log units above the FMQ buffer) and also more oxidised than the mantle wedge beneath subduction zone volcanoes. What emerges is a novel view of the oxidation state of the mantle, in which large heterogeneities exist both vertically and laterally.

We further argue that mantle plumes play a key role in the deep oxygen cycle, providing a counterflow to subduction zones by channelling oxidised material out of the deep Earth. This can help to explain why the mean oxidation state of the upper mantle has changed little since the Archean, despite several billion years of subduction of oxidised material. Our findings also have implications for the interpretation of low seismic velocity anomalies beneath hotspot volcanoes, as these might reflect the presence of more oxidised mantle as well as higher mantle temperatures. The more oxidised conditions imply in turn that carbonate redox melting underneath hotspots should take place at much greater depths than underneath mid-ocean ridges.

ACKNOWLEDGEMENTS

Analytical work was carried out at the Diamond Light Source using beamline I18 (proposal number SP17250-1) with invaluable support received from Konstantin Ignatyev. YM acknowledges support from the CNRS (projet INSU-TelluS-SYSTER). CO is supported by the NERC Centre for Observation and Modelling of Earthquakes, Volcanoes and Tectonics. BS is supported by Labex VOLTAIRE (ANR-10-LABX-100-01). We thank Elizabeth Cottrell and Marc Hirschmann for constructive and beneficial comments on the original manuscript.

REFERENCES

Alt, J.C., Shanks, W.C., Jackson, M.C., 1993. Cycling of sulfur in subduction zones: The geochemistry of sulfur in the Mariana Island Arc and back-arc trough. Earth and Planetary Science Letters 119, 477–494. https://doi.org/10.1016/0012-821X(93)90057-G

Anderson, A.T., Brown, G.G., 1993. CO_2 contents and formation pressures of some Kilauean melt inclusions. American Mineralogist 78, 794–803.

Anderson, A.T., Wright, R., 1972. Phenocrysts and glass inclusions and their bearing on oxidation and mixing of basaltic magmas, Kilauea Volcano, Hawaii 57, 188–216.

Arculus, R.J., 1985. Oxidation status of the mantle: past and present. Annu. Rev. Earth Planet. Sci. 13, 75–95. https://doi.org/10.1146/annurev.ea.13.050185.000451

Bénard, A., Klimm, K., Woodland, A.B., Arculus, R.J., Wilke, M., Botcharnikov, R.E., Shimizu, N., Nebel, O., Rivard, C., Ionov, D.A., 2018. Oxidising agents in sub-arc mantle melts link slab devolatilisation and arc magmas. Nature Communications 9, 3500. https://doi.org/10.1038/s41467-018-05804-2

Berry, A.J., O'Neill, H.S.C., Jayasuriya, K.D., Campbell, S.J., Foran, G.J., 2003. XANES calibrations for the oxidation state of iron in a silicate glass. American Mineralogist 88, 967–977. https://doi.org/10.2138/am-2003-0704

Berry, A.J., Stewart, G.A., O'Neill, H.St.C., Mallmann, G., Mosselmans, J.F.W., 2018. A re-assessment of the oxidation state of iron in MORB glasses. Earth and Planetary Science Letters 483, 114–123. https://doi.org/10.1016/j.epsl.2017.11.032

Bezos, A., Humler, E., 2005. The Fe3 /Sigma Fe ratios of MORB glasses and their implications for mantle melting. Geochimica Et Cosmochimica Acta 69, 711–725.

Birner, S.K., Cottrell, E., Warren, J.M., Kelley, K.A., Davis, F.A., 2018. Peridotites and basalts reveal broad congruence between two independent records of mantle fO2 despite local redox heterogeneity. Earth and Planetary Science Letters 494, 172–189. https://doi.org/10.1016/j.epsl.2018.04.035

Birner, S.K., Warren, J.M., Cottrell, E., Davis, F.A., Kelley, K.A., Falloon, T.J., 2017. Forearc Peridotites from Tonga Record Heterogeneous Oxidation of the Mantle following Subduction Initiation. J Petrology 58, 1755–1780. https://doi.org/10.1093/petrology/egx072

577 Blank, J.G., Brooker, R.A., 1994. Experimental studies of carbon dioxide in silicate melts;
578 solubility, speciation, and stable carbon isotope behavior. Reviews in Mineralogy and
579 Geochemistry 30, 157–186.
580 Botcharnikov, R.E., Linnen, R.L., Wilke, M., Holtz, F., Jugo, P.J., Berndt, J., 2011. High gold
581 concentrations in sulphide-bearing magma under oxidizing conditions. Nature
582 Geoscience 4, 112–115. https://doi.org/10.1038/ngeo1042
583 Brandon, A.D., Draper, D.S., 1996. Constraints on the origin of the oxidation state of mantle
584 overlying subduction zones: An example from Simcoe, Washington, USA. Geochimica
585 et Cosmochimica Acta 60, 1739–1749. https://doi.org/10.1016/0016-7037(96)00056-7
586 Brounce, M., Stolper, E., Eiler, J., 2017. Redox variations in Mauna Kea lavas, the oxygen
587 fugacity of the Hawaiian plume, and the role of volcanic gases in Earth's oxygenation.
588 PNAS 114, 8997–9002. https://doi.org/10.1073/pnas.1619527114
589 Bryndzia, L.T., Wood, B.J., 1990. Oxygen thermobarometry of abyssal spinel peridotites; the
590 redox state and C-O-H volatile composition of the Earth's sub-oceanic upper mantle.
591 Am J Sci 290, 1093–1116. https://doi.org/10.2475/ajs.290.10.1093
592 Bucholz, C.E., Gaetani, G.A., Behn, M.D., Shimizu, N., 2013. Post-entrapment modification
593 of volatiles and oxygen fugacity in olivine-hosted melt inclusions. Earth and Planetary
594 Science Letters 374, 145–155. https://doi.org/10.1016/j.epsl.2013.05.033
595 Burgisser, A., Scaillet, B., 2007. Redox evolution of a degassing magma rising to the surface.
596 Nature 445, 194–197.
597 Bykova, E., Dubrovinsky, L., Dubrovinskaia, N., Bykov, M., McCammon, C., Ovsyannikov,
598 S.V., Liermann, H.-P., Kupenko, I., Chumakov, A.I., Rüffer, R., Hanfland, M.,
599 Prakapenka, V., 2016. Structural complexity of simple Fe_2O_3 at high pressures and
600 temperatures. Nature Communications 7, 10661.
601 https://doi.org/10.1038/ncomms10661
602 Canil, D., O'Neill, H.St.C., Pearson, D.G., Rudnick, R.L., McDonough, W.F., Carswell, D.A.,
603 1994. Ferric iron in peridotites and mantle oxidation states. Earth and Planetary Science
604 Letters 123, 205–220. https://doi.org/10.1016/0012-821X(94)90268-2
605 Carmichael, I.S.E., 1991. The redox states of basic and silicic magmas: a reflection of their
606 source regions? Contr. Mineral. and Petrol. 106, 129–141.
607 https://doi.org/10.1007/BF00306429
608 Carmichael, I.S.E., Ghiorso, M.S., 1986. Oxidation-reduction relations in basic magma: a case
609 for homogeneous equilibria. Earth and Planetary Science Letters 78, 200–210.
610 https://doi.org/10.1016/0012-821X(86)90061-0
611 Chauvel, C., Hofmann, A.W., Vidal, P., 1992. himu-em: The French Polynesian connection.
612 Earth and Planetary Science Letters 110, 99–119. https://doi.org/10.1016/0012-
613 821X(92)90042-T
614 Christensen, B.P., Holm, P.M., Jambon, A., Wilson, J.R., 2001. Helium, argon and lead
615 isotopic composition of volcanics from Santo Antão and Fogo, Cape Verde Islands.
616 Chemical Geology 178, 127–142. https://doi.org/10.1016/S0009-2541(01)00261-3
617 Christie, D.M., Carmichael, I.S.E., Langmuir, C.H., 1986. Oxidation states of mid-ocean ridge
618 basalt glasses. Earth and Planetary Science Letters 79, 397–411.
619 https://doi.org/10.1016/0012-821X(86)90195-0
620 Cottrell, E., Kelley, K.A., 2011. The oxidation state of Fe in MORB glasses and the oxygen
621 fugacity of the upper mantle. Earth and Planetary Science Letters 305, 270–282.
622 https://doi.org/10.1016/j.epsl.2011.03.014
623 Cottrell, E., Kelley, K.A., Lanzirotti, A., Fischer, R.A., 2009. High-precision determination of
624 iron oxidation state in silicate glasses using XANES. Chemical Geology 268, 167–179.
625 https://doi.org/10.1016/j.chemgeo.2009.08.008

626 Cottrell, E., Lanzirotti, A., Mysen, B., Birner, S., Kelley, K.A., Botcharnikov, R., Davis, F.A.,
627 Newville, M., 2018. A Mössbauer-based XANES calibration for hydrous basalt glasses
628 reveals radiation-induced oxidation of Fe. American Mineralogist 103, 489–501.
629 https://doi.org/10.2138/am-2018-6268
630 Danyushevsky, L.V., 2001. The effect of small amounts of H2O on crystallisation of mid-ocean
631 ridge and backarc basin magmas. Journal of Volcanology and Geothermal Research
632 110, 265–280. https://doi.org/10.1016/S0377-0273(01)00213-X
633 Danyushevsky, L.V., Plechov, P., 2011. Petrolog3: Integrated software for modeling
634 crystallization processes. Geochemistry, Geophysics, Geosystems 12, n/a–n/a.
635 https://doi.org/10.1029/2011GC003516
636 Day, J.M.D., Hilton, D.R., 2011. Origin of 3He/4He ratios in HIMU-type basalts constrained
637 from Canary Island lavas. Earth and Planetary Science Letters 305, 226–234.
638 https://doi.org/10.1016/j.epsl.2011.03.006
639 Day, J.M.D., Pearson, D.G., Macpherson, C.G., Lowry, D., Carracedo, J.C., 2010. Evidence
640 for distinct proportions of subducted oceanic crust and lithosphere in HIMU-type
641 mantle beneath El Hierro and La Palma, Canary Islands. Geochimica et Cosmochimica
642 Acta 74, 6565–6589. https://doi.org/10.1016/j.gca.2010.08.021
643 Doucelance, R., Escrig, S., Moreira, M., Gariépy, C., Kurz, M.D., 2003. Pb-Sr-He isotope and
644 trace element geochemistry of the Cape Verde Archipelago. Geochimica et
645 Cosmochimica Acta 67, 3717–3733. https://doi.org/10.1016/S0016-7037(03)00161-3
646 Farges, F., 2001. Crystal chemistry of iron in natural grandidierites: an X-ray absorption fine-
647 structure spectroscopy study. Phys Chem Min 28, 619–629.
648 https://doi.org/10.1007/s002690100170
649 French, S.W., Romanowicz, B., 2015. Broad plumes rooted at the base of the Earth's mantle
650 beneath major hotspots. Nature 525, 95–99. https://doi.org/10.1038/nature14876
651 Frost, B.R., 1991. Introduction to oxygen fugacity and its petrologic importance. Reviews in
652 Mineralogy and Geochemistry 25, 1–9.
653 Frost, D.J., McCammon, C.A., 2008. The Redox State of Earth's Mantle. Annual Review of
654 Earth and Planetary Sciences 36, 389–420.
655 https://doi.org/10.1146/annurev.earth.36.031207.124322
656 Gaetani, G.A., O'Leary, J.A., Shimizu, N., Bucholz, C.E., Newville, M., 2012. Rapid
657 reequilibration of H2O and oxygen fugacity in olivine-hosted melt inclusions. Geology
658 40, 915–918. https://doi.org/10.1130/G32992.1
659 Gaillard, F., Scaillet, B., Arndt, N.T., 2011. Atmospheric oxygenation caused by a change in
660 volcanic degassing pressure. Nature 478, 229–232.
661 https://doi.org/10.1038/nature10460
662 Gaillard, F., Scaillet, B., Pichavant, M., Iacono-Marziano, G., 2015. The redox geodynamics
663 linking basalts and their mantle sources through space and time. Chemical Geology
664 418, 217–233. https://doi.org/10.1016/j.chemgeo.2015.07.030
665 Gómez-Ulla, A., 2018. Historical eruptions of Lanzarote, Canary Islands: Inference of magma
666 source and melt generation from olivine and its melt inclusions. University of Clermont
667 - Auvergne, Clermont-Ferrand.
668 Gómez-Ulla, A., Sigmarsson, O., Gudfinnsson, G.H., 2017. Trace element systematics of
669 olivine from historical eruptions of Lanzarote, Canary Islands: Constraints on mantle
670 source and melting mode. Chemical Geology 449, 99–111.
671 https://doi.org/10.1016/j.chemgeo.2016.11.021
672 Hartley, M.E., Shorttle, O., Maclennan, J., Moussallam, Y., Edmonds, M., 2017. Olivine-
673 hosted melt inclusions as an archive of redox heterogeneity in magmatic systems. Earth
674 and Planetary Science Letters 479, 192–205. https://doi.org/10.1016/j.epsl.2017.09.029

675 Hauri, E., 2002. SIMS analysis of volatiles in silicate glasses, 2: isotopes and abundances in
676 Hawaiian melt inclusions. Chemical Geology 183, 115–141.
677 https://doi.org/10.1016/S0009-2541(01)00374-6
678 Hauri, E.H., 1996. Major-element variability in the Hawaiian mantle plume. Nature 382, 415–
679 419. https://doi.org/10.1038/382415a0
680 Helz, R.T., Cottrell, E., Brounce, M.N., Kelley, K.A., 2017. Olivine-melt relationships and
681 syneruptive redox variations in the 1959 eruption of Kīlauea Volcano as revealed by
682 XANES. Journal of Volcanology and Geothermal Research 333–334, 1–14.
683 https://doi.org/10.1016/j.jvolgeores.2016.12.006
684 Herzberg, C., Asimow, P.D., 2015. PRIMELT3 MEGA.XLSM software for primary magma
685 calculation: Peridotite primary magma MgO contents from the liquidus to the solidus.
686 Geochemistry, Geophysics, Geosystems 16, 563–578.
687 https://doi.org/10.1002/2014GC005631
688 Hiltona, D.R., Macphersona, C.G., Elliottb, T.R., 2000. Helium isotope ratios in mafic
689 phenocrysts and geothermal fluids from La Palma, the Canary Islands (Spain):
690 implications for HIMU mantle sources. Geochimica et Cosmochimica Acta 64, 2119–
691 2132. https://doi.org/10.1016/S0016-7037(00)00358-6
692 Hofmann, A.W., White, W.M., 1982. Mantle plumes from ancient oceanic crust. Earth and
693 Planetary Science Letters 57, 421–436. https://doi.org/10.1016/0012-821X(82)90161-
694 3
695 Holloway, J.R., Burnham, C.W., 1972. Melting Relations of Basalt with Equilibrium Water
696 Pressure Less Than Total Pressure. J Petrology 13, 1–29.
697 https://doi.org/10.1093/petrology/13.1.1
698 Hu, Q., Kim, D.Y., Liu, J., Meng, Y., Yang, L., Zhang, D., Mao, W.L., Mao, H., 2017.
699 Dehydrogenation of goethite in Earth's deep lower mantle. PNAS 114, 1498–1501.
700 https://doi.org/10.1073/pnas.1620644114
701 Hu, Q., Kim, D.Y., Yang, W., Yang, L., Meng, Y., Zhang, L., Mao, H.-K., 2016. FeO_2 and
702 FeOOH under deep lower-mantle conditions and Earth's oxygen–hydrogen cycles.
703 Nature 534, 241–244. https://doi.org/10.1038/nature18018
704 Iacono-Marziano, G., Morizet, Y., Le Trong, E., Gaillard, F., 2012. New experimental data and
705 semi-empirical parameterization of H2O–CO2 solubility in mafic melts. Geochimica et
706 Cosmochimica Acta 97, 1–23. https://doi.org/10.1016/j.gca.2012.08.035
707 Ii, C.J.C., Faul, U.H., David, E.C., Berry, A.J., Jackson, I., 2018. Redox-influenced seismic
708 properties of upper-mantle olivine. Nature 555, 355–358.
709 https://doi.org/10.1038/nature25764
710 Jarosewich, E., Parkes, A.S., Wiggins, L.B., 1979. Microprobe Analyses of Four Natural
711 Glasses and One Mineral: An Interlaboratory Study of Precision and Accuracy.
712 Smithsonian Contributions to the Earth Sciences 22, 53–67.
713 Jégo, S., Dasgupta, R., 2014. The Fate of Sulfur During Fluid-Present Melting of Subducting
714 Basaltic Crust at Variable Oxygen Fugacity. J Petrology 55, 1019–1050.
715 https://doi.org/10.1093/petrology/egu016
716 Jégo, S., Dasgupta, R., 2013. Fluid-present melting of sulfide-bearing ocean-crust:
717 Experimental constraints on the transport of sulfur from subducting slab to mantle
718 wedge. Geochimica et Cosmochimica Acta 110, 106–134.
719 https://doi.org/10.1016/j.gca.2013.02.011
720 Jugo, P.J., Wilke, M., Botcharnikov, R.E., 2010. Sulfur K-edge XANES analysis of natural and
721 synthetic basaltic glasses: Implications for S speciation and S content as function of
722 oxygen fugacity. Geochimica et Cosmochimica Acta 74, 5926–5938.
723 https://doi.org/10.1016/j.gca.2010.07.022

724 Kelley, K.A., Cottrell, E., 2012. The influence of magmatic differentiation on the oxidation
725 state of Fe in a basaltic arc magma. Earth and Planetary Science Letters 329–330, 109–
726 121. https://doi.org/10.1016/j.epsl.2012.02.010
727 Kress, V.C., Carmichael, I.S.E., 1991. The compressibility of silicate liquids containing Fe2O3
728 and the effect of composition, temperature, oxygen fugacity and pressure on their redox
729 states. Contr. Mineral. and Petrol. 108, 82–92. https://doi.org/10.1007/BF00307328
730 Kress, V.C., Carmichael, I.S.E., 1988. Stoichiometry of the iron oxidation reaction in silicate
731 melts. American Mineralogist 73, 1267–1274.
732 Lange, R.L., Carmichael, I.S.E., 1990. Thermodynamic properties of silicate liquids with
733 emphasis on density, thermal expansion and compressibility. Reviews in Mineralogy
734 and Geochemistry 24, 25–64.
735 Longpré, M.-A., Stix, J., Klügel, A., Shimizu, N., 2017. Mantle to surface degassing of carbon-
736 and sulphur-rich alkaline magma at El Hierro, Canary Islands. Earth and Planetary
737 Science Letters 460, 268–280. https://doi.org/10.1016/j.epsl.2016.11.043
738 Mallmann, G., O'Neill, H.S.C., 2009. The Crystal/Melt Partitioning of V during Mantle
739 Melting as a Function of Oxygen Fugacity Compared with some other Elements (Al, P,
740 Ca, Sc, Ti, Cr, Fe, Ga, Y, Zr and Nb). J. Petrology 50, 1765–1794.
741 https://doi.org/10.1093/petrology/egp053
742 Massare, D., Métrich, N., Clocchiatti, R., 2002. High-temperature experiments on silicate melt
743 inclusions in olivine at 1 atm: inference on temperatures of homogenization and H2O
744 concentrations. Chemical Geology, Melt Inclusions at the Millennium: Toward a
745 Deeper Understanding of Magmatic Processes 183, 87–98.
746 https://doi.org/10.1016/S0009-2541(01)00373-4
747 Métrich, N., Berry, A.J., O'Neill, H.St.C., Susini, J., 2009. The oxidation state of sulfur in
748 synthetic and natural glasses determined by X-ray absorption spectroscopy.
749 Geochimica et Cosmochimica Acta 73, 2382–2399.
750 https://doi.org/10.1016/j.gca.2009.01.025
751 Millet, M.-A., Doucelance, R., Schiano, P., David, K., Bosq, C., 2008. Mantle plume
752 heterogeneity versus shallow-level interactions: A case study, the São Nicolau Island,
753 Cape Verde archipelago. Journal of Volcanology and Geothermal Research 176, 265–
754 276. https://doi.org/10.1016/j.jvolgeores.2008.04.003
755 Mosbah, M., Metrich, N., Massiot, P., 1991. PIGME fluorine determination using a nuclear
756 microprobe with application to glass inclusions. Nuclear Instruments and Methods in
757 Physics Research Section B: Beam Interactions with Materials and Atoms 58, 227–231.
758 https://doi.org/10.1016/0168-583X(91)95592-2
759 Moussallam, Y., Edmonds, M., Scaillet, B., Peters, N., Gennaro, E., Sides, I., Oppenheimer,
760 C., 2016. The impact of degassing on the oxidation state of basaltic magmas: A case
761 study of Kīlauea volcano. Earth and Planetary Science Letters 450, 317–325.
762 https://doi.org/10.1016/j.epsl.2016.06.031
763 Moussallam, Y., Oppenheimer, C., Scaillet, B., Gaillard, F., Kyle, P., Peters, N., Hartley, M.,
764 Berlo, K., Donovan, A., 2014. Tracking the changing oxidation state of Erebus
765 magmas, from mantle to surface, driven by magma ascent and degassing. Earth and
766 Planetary Science Letters 393, 200–209. https://doi.org/10.1016/j.epsl.2014.02.055
767 O'Neill, H.St.C., Berry, A.J., Mallmann, G., 2018. The oxidation state of iron in Mid-Ocean
768 Ridge Basaltic (MORB) glasses: Implications for their petrogenesis and oxygen
769 fugacities. Earth and Planetary Science Letters 504, 152–162.
770 https://doi.org/10.1016/j.epsl.2018.10.002
771 Parkinson, I.J., Arculus, R.J., 1999. The redox state of subduction zones: insights from arc-
772 peridotites. Chemical Geology 160, 409–423. https://doi.org/10.1016/S0009-
773 2541(99)00110-2

774 Prescher, C., McCammon, C., Dubrovinsky, L., 2012. MossA: a program for analyzing energy-
775 domain Mössbauer spectra from conventional and synchrotron sources. J Appl Cryst, J
776 Appl Crystallogr 45, 329–331. https://doi.org/10.1107/S0021889812004979
777 Prouteau, G., Scaillet, B., 2013. Experimental Constraints on Sulphur Behaviour in Subduction
778 Zones: Implications for TTG and Adakite Production and the Global Sulphur Cycle
779 since the Archean. J Petrology 54, 183–213. https://doi.org/10.1093/petrology/egs067
780 Rancourt, D.G., 1989. Accurate site populations from Mössbauer spectroscopy. Nuclear
781 Instruments and Methods in Physics Research Section B: Beam Interactions with
782 Materials and Atoms 44, 199–210. https://doi.org/10.1016/0168-583X(89)90428-X
783 Rhodes, J.M., Vollinger, M.J., 2005. Ferric/ferrous ratios in 1984 Mauna Loa lavas: a
784 contribution to understanding the oxidation state of Hawaiian magmas. Contrib Mineral
785 Petrol 149, 666–674. https://doi.org/10.1007/s00410-005-0662-y
786 Roeder, P.L., Thornber, C., Poustovetov, A., Grant, A., 2003. Morphology and composition of
787 spinel in Pu'u 'O'o lava (1996–1998), Kilauea volcano, Hawaii. Journal of
788 Volcanology and Geothermal Research 123, 245–265. https://doi.org/10.1016/S0377-
789 0273(02)00508-5
790 Rohrbach, A., Schmidt, M.W., 2011. Redox freezing and melting in the Earth/'s deep mantle
791 resulting from carbon-iron redox coupling. Nature 472, 209–212.
792 https://doi.org/10.1038/nature09899
793 Rowe, M.C., Kent, A.J.R., Nielsen, R.L., 2007. Determination of sulfur speciation and
794 oxidation state of olivine hosted melt inclusions. Chemical Geology 236, 303–322.
795 https://doi.org/10.1016/j.chemgeo.2006.10.007
796 Foley, S. F. 2010. A Reappraisal of Redox Melting in the Earth's Mantle as a Function of
797 Tectonic Setting and Time. Journal of Petrology 52, 1363–1391.
798 https://doi.org/10.1093/petrology/egq061
799 Shishkina, T.A., Botcharnikov, R.E., Holtz, F., Almeev, R.R., Jazwa, A.M., Jakubiak, A.A.,
800 2014. Compositional and pressure effects on the solubility of H2O and CO2 in mafic
801 melts. Chemical Geology 388, 112–129.
802 https://doi.org/10.1016/j.chemgeo.2014.09.001
803 Shorttle, O., Moussallam, Y., Hartley, M.E., Maclennan, J., Edmonds, M., Murton, B.J., 2015.
804 Fe-XANES analyses of Reykjanes Ridge basalts: Implications for oceanic crust's role
805 in the solid Earth oxygen cycle. Earth and Planetary Science Letters 427, 272–285.
806 https://doi.org/10.1016/j.epsl.2015.07.017
807 Sorbadere, F., Laurenz, V., Frost, D.J., Wenz, M., Rosenthal, A., McCammon, C., Rivard, C.,
808 2018. The behaviour of ferric iron during partial melting of peridotite. Geochimica et
809 Cosmochimica Acta 239, 235–254. https://doi.org/10.1016/j.gca.2018.07.019
810 Stagno, V., Ojwang, D.O., McCammon, C.A., Frost, D.J., 2013. The oxidation state of the
811 mantle and the extraction of carbon from Earth/'s interior. Nature 493, 84–88.
812 https://doi.org/10.1038/nature11679
813 Steele-Macinnis, M., Esposito, R., Bodnar, R.J., 2011. Thermodynamic Model for the Effect
814 of Post-entrapment Crystallization on the H2O–CO2 Systematics of Vapor-saturated,
815 Silicate Melt Inclusions. J Petrology 52, 2461–2482.
816 https://doi.org/10.1093/petrology/egr052
817 Streltsov, S.S., Shorikov, A.O., Skornyakov, S.L., Poteryaev, A.I., Khomskii, D.I., 2017.
818 Unexpected 3+ valence of iron in FeO 2 , a geologically important material lying "in
819 between" oxides and peroxides. Scientific Reports 7, 13005.
820 https://doi.org/10.1038/s41598-017-13312-4
821 Taylor, W.R., Green, D.H., 1988. Measurement of reduced peridotite-C-O-H solidus and
822 implications for redox melting of the mantle. Nature 332, 349.
823 https://doi.org/10.1038/332349a0

824 Tomkins, A.G., Evans, K.A., 2015. Separate zones of sulfate and sulfide release from
825 subducted mafic oceanic crust. Earth and Planetary Science Letters 428, 73–83.
826 https://doi.org/10.1016/j.epsl.2015.07.028
827 Toplis, M.J., 2005. The thermodynamics of iron and magnesium partitioning between olivine
828 and liquid: criteria for assessing and predicting equilibrium in natural and experimental
829 systems. Contrib Mineral Petrol 149, 22–39. https://doi.org/10.1007/s00410-004-0629-
830 4
831 White, W.M., 2015. Probing the Earth's Deep Interior through Geochemistry. Geochemical
832 Perspectives 4, 95–96.
833 Wilke, M., Farges, F., Petit, P.-E., Brown, G.E., Martin, F., 2001. Oxidation state and
834 coordination of Fe in minerals: An Fe K-XANES spectroscopic study. American
835 Mineralogist 86, 714–730. https://doi.org/10.2138/am-2001-5-612
836 Wilke, M., Jugo, P.J., Klimm, K., Susini, J., Botcharnikov, R., Kohn, S.C., Janousch, M., 2008.
837 The origin of S4 detected in silicate glasses by XANES. American Mineralogist 93,
838 235–240. https://doi.org/10.2138/am.2008.2765
839 Wilke, M., Partzsch, G.M., Bernhardt, R., Lattard, D., 2004. Determination of the iron
840 oxidation state in basaltic glasses using XANES at the K-edge. Chemical Geology, 7th
841 Silicate Melt Workshop 213, 71–87. https://doi.org/10.1016/j.chemgeo.2004.08.034
842 Woodland, A.B., Koch, M., 2003. Variation in oxygen fugacity with depth in the upper mantle
843 beneath the Kaapvaal craton, Southern Africa. Earth and Planetary Science Letters 214,
844 295–310. https://doi.org/10.1016/S0012-821X(03)00379-0
845 Zhang, H.L., Cottrell, E., Solheid, P.A., Kelley, K.A., Hirschmann, M.M., 2018. Determination
846 of Fe3+/ΣFe of XANES basaltic glass standards by Mössbauer spectroscopy and its
847 application to the oxidation state of iron in MORB. Chemical Geology 479, 166–175.
848 https://doi.org/10.1016/j.chemgeo.2018.01.006
849 Zhao, D., 2007. Seismic images under 60 hotspots: Search for mantle plumes. Gondwana
850 Research 12, 335–355. https://doi.org/10.1016/j.gr.2007.03.001
851